

The stably stratified Taylor–Couette flow is always unstable except for solid-body rotation

Junho Park[†] and Paul Billant

LadHyX, CNRS, Ecole Polytechnique, F-91128 Palaiseau CEDEX, France

(Received 18 October 2012; revised 19 February 2013; accepted 8 April 2013)

The stability of the flow between two concentric cylinders is studied numerically and analytically when the fluid is stably stratified. We show that such flow is unstable when the angular velocity $\Omega(r)$ increases along the radial direction, a regime never explored before. The instability is highly non-axisymmetric and involves the resonance of two families of inertia–gravity waves like for the strato-rotational instability. The growth rate is maximum when only the outer cylinder is rotating and goes to zero when $\Omega(r)$ is constant. The sufficient condition for linear, inviscid instability derived previously, $d\Omega^2/dr < 0$, is therefore extended to $d\Omega^2/dr \neq 0$, meaning that only the regime of solid-body rotation is stable in stratified fluids. A Wentzel–Kramers–Brillouin–Jeffreys (WKBJ) analysis in the inviscid limit, confirmed by the numerical results, shows that the instability occurs only when the Froude number is below a critical value and only for a particular band of azimuthal wavenumbers. It is also demonstrated that the instability originates from a reversal of the radial group velocity of the waves, or equivalently from a wave over-reflection phenomenon. The instability persists in the presence of viscous effects.

Key words: instability, stratified flows, vortex flows

1. Introduction

The Taylor–Couette flow is a canonical and popular flow that has led to a very large number of studies and significant advances in the understanding of fluid stability and transitions to chaos and turbulence (Andereck, Liu & Swinney 1986; Dubrulle *et al.* 2005a). It consists of the sheared flow between two independently rotating concentric cylinders. The base flow is steady and axisymmetric with angular velocity

$$\Omega(r) = A + \frac{B}{r^2}, \quad (1.1)$$

with $A = (r_o^2\Omega_o - r_i^2\Omega_i)/(r_o^2 - r_i^2)$ and $B = r_i^2r_o^2(\Omega_i - \Omega_o)/(r_o^2 - r_i^2)$, where (r_i, r_o) and (Ω_i, Ω_o) are the radius and the angular velocity of the inner and outer cylinders, respectively.

According to the Rayleigh criterion, such base flow is unstable to the centrifugal instability (CI) in an inviscid fluid if the angular momentum decreases in the radial direction, $d(r^2\Omega)/dr < 0$, or equivalently $\mu < \eta^2$, where $\mu = \Omega_o/\Omega_i$ and $\eta = r_i/r_o$ are the two classical control parameters of the Taylor–Couette flow. The Rayleigh

[†] Email address for correspondence: junho.park@ladhyx.polytechnique.fr

criterion remains valid in the presence of a stable density stratification along the axial (vertical) direction (Ooyama 1966; Billant & Gallaire 2005). Such flow, which combines horizontal shear and vertical stratification, is of great interest in geophysics and astrophysics: for example, the stratified Taylor–Couette flow serves as a model for instabilities in equatorial oceans (Hua, Moore & Le Gentil 1997b), or in Keplerian flows in accretion disks (Dubrulle *et al.* 2005b).

Early studies of the stratified Taylor–Couette flow have mostly been performed when the outer cylinder is at rest ($\mu = 0$) (Withjack & Chen 1974; Boubnov, Gledzer & Hopfinger 1995; Hua, Le Gentil & Orlandi 1997a; Caton, Janiaud & Hopfinger 2000). These authors reported that the stratification in viscous fluid stabilizes the flows, as one might intuitively expect since the buoyancy force is restoring. Surprisingly, however, Molemaker, McWilliams & Yavneh (2001) and Yavneh, McWilliams & Molemaker (2001) have shown that the Taylor–Couette flow with sufficiently strong stratification remains unstable beyond the Rayleigh threshold $\mu = \eta^2$. They found that a sufficient condition for inviscid instability in stratified fluids is actually $d\Omega^2/dr < 0$ corresponding to $\mu < 1$. The dominant instability beyond the Rayleigh line ($\eta^2 < \mu < 1$) is non-axisymmetric and therefore different from the axisymmetric Taylor vortices of the CI. This instability, now referred as the strato-rotational instability (SRI) (Dubrulle *et al.* 2005b), comes from the resonant interaction between two boundary-trapped waves on each cylinder (Molemaker *et al.* 2001; Yavneh *et al.* 2001; Le Dizès & Riedinger 2010). However, Le Dizès & Riedinger (2010) have found that the flow remains unstable when the outer cylinder is absent but the SRI transforms to a radiative instability (Billant & Le Dizès 2009; Le Dizès & Billant 2009; Riedinger, Meunier & Le Dizès 2010; Riedinger, Le Dizès & Meunier 2011). Stability analysis (Shalybkov & Rüdiger 2005) and experiments (Le Bars & Le Gal 2007) have shown that the threshold for the SRI in viscous fluids is $\mu \approx \eta$, so that the flow is stable for $\eta \lesssim \mu < 1$.

Even though the condition $d\Omega^2/dr < 0$ ($\mu < 1$) has been proposed as only a sufficient condition for inviscid instability in stratified fluids (Molemaker *et al.* 2001; Yavneh *et al.* 2001), the regime where the angular velocity increases with r ($\mu > 1$) has been generally thought to be stable for the stratified Taylor–Couette flow (Molemaker *et al.* 2001; Yavneh *et al.* 2001; Le Dizès & Riedinger 2010). To our knowledge, however, this regime has not been explored. Nevertheless, Vanneste & Yavneh (2007) have studied the stability of the rotating stratified horizontal plane Couette flow in a channel, which shares many similarities with the stratified Taylor–Couette flow. In particular, anticyclonic and cyclonic shears correspond to $\mu < 1$ and $\mu > 1$, respectively. Interestingly, they have shown by means of an asymptotic analysis in the limit of small Rossby number that such plane Couette flow is unconditionally unstable, i.e. for both anticyclonic and cyclonic shears. However, the growth rate is reported to be much smaller in the cyclonic case than in the anticyclonic case.

Another related study concerns the stability of a columnar vertical Rankine vortex in a stratified rotating fluid. Park & Billant (2012) have shown that such a vortex is unstable to a radiative instability in the centrifugally stable anticyclonic regime, $-1 < Ro < 0$, where $Ro = \Omega_v/\Omega_b$ is the Rossby number, with Ω_v the angular velocity in the vortex core and Ω_b the angular velocity of the background rotation. (Note that the meanings of ‘anticyclonic’ for a vortex and for the plane Couette flow differ (Vanneste & Yavneh 2007).) The potential flow outside the vortex core has linearized perturbation equations equivalent to those of the Taylor–Couette flow if the Rossby

number is set to

$$Ro = \frac{1 - \mu}{\mu - \eta^2}. \tag{1.2}$$

This relation shows that the regime $\mu > 1$ for the Taylor–Couette flow corresponds to $-1 \leq Ro < 0$ for a vortex. Although the boundary conditions differ completely between the two flows, this suggests that the regime $\mu > 1$ might be unstable since the radiative and SRI instabilities are closely related (Le Dizès & Riedinger 2010).

In this paper, we shall show that the stratified Taylor–Couette flow for $\mu > 1$ is indeed also unstable to the SRI. In contrast to the plane Couette flow (Vanneste & Yavneh 2007), the growth rates in the regimes $\mu < 1$ and $\mu > 1$ are comparable. Strikingly, we shall see that the stratified inviscid Taylor–Couette flow is stable only in the limit of solid-body rotation ($\mu = 1$).

The paper is organized as follows. The problem is formulated in § 2. A typical example of instability is first described in § 3. In § 4, a Wentzel–Kramers–Brillouin–Jeffreys (WKBJ) asymptotic analysis explains the instability mechanism and provides general conditions for instability. The effects of the main parameters of the problem are investigated numerically in § 5.

2. Problem formulation

We consider the linear stability of the base flow (1.1) in a stratified fluid with a constant Brunt–Väisälä frequency $N = \sqrt{-(g/\rho_0)\partial\bar{\rho}/\partial z}$, where g is the gravity, $\bar{\rho}(z)$ the basic density profile along the vertical direction z and ρ_0 a reference density. The perturbations of velocity $\mathbf{u}' = (u'_r, u'_\theta, u'_z)$ in cylindrical coordinates (r, θ, z) , pressure p' and density ρ' are written in the form $(\mathbf{u}', p', \rho') = (u_r(r), u_\theta(r), u_z(r), p(r), \rho(r))e^{i(kz+m\theta-\omega t)} + \text{c.c.}$, where ω is the complex eigenfrequency, m the azimuthal wavenumber and k the vertical wavenumber. Under the Boussinesq approximation, the linearized equations of momentum, continuity and density conservation for the perturbations are

$$isu_r - 2\Omega u_\theta = -\frac{1}{\rho_0} \frac{dp}{dr} + \nu \left[\nabla^2 u_r - \frac{u_r}{r^2} - \frac{2im}{r^2} u_\theta \right], \tag{2.1}$$

$$isu_\theta + Zu_r = -\frac{imp}{\rho_0 r} + \nu \left[\nabla^2 u_\theta - \frac{u_\theta}{r^2} + \frac{2im}{r^2} u_r \right], \tag{2.2}$$

$$isu_z = -\frac{ik}{\rho_0} p - \frac{g}{\rho_0} \rho + \nu \nabla^2 u_z, \tag{2.3}$$

$$\frac{1}{r} \frac{d(ru_r)}{dr} + \frac{imu_\theta}{r} + iku_z = 0, \tag{2.4}$$

$$is\rho - \frac{N^2 \rho_0}{g} u_z = D \nabla^2 \rho, \tag{2.5}$$

where $s = -\omega + m\Omega$ is the Doppler-shifted frequency, $Z = (1/r)d(r^2\Omega)/dr$ the axial vorticity of the base flow, $\nabla^2 = d^2/dr^2 + (1/r)d/dr - (k^2 + m^2/r^2)$ the Laplacian operator, ν the kinematic viscosity and D the molecular diffusivity of the stratifying agent. The boundary conditions are $u_r = u_\theta = u_z = d\rho/dr = 0$ at both cylinders $r = r_i, r_o$. Owing to the symmetry $\omega(k, m) = \omega(-k, m) = -\omega^*(-k, -m)$, we consider hereafter only positive k and m .

In the inviscid and non-diffusive limit $\nu = D = 0$, the equations (2.1)–(2.5) can be reduced to a single equation for the radial velocity u_r :

$$\frac{d^2 u_r}{dr^2} + \left(\frac{1}{r} - \frac{Q'}{Q} \right) \frac{du_r}{dr} + \left[-\frac{k^2}{N^2 - s^2} \Delta - \frac{m^2}{r^2} - \frac{mrQ}{s} \left(\frac{Z}{r^2 Q} \right)' + Q \left(\frac{1}{rQ} \right)' \right] u_r = 0, \tag{2.6}$$

where $Q(r) = m^2/r^2 - k^2 s^2/(N^2 - s^2)$, $\Delta(r) = \phi - s^2$, $\phi = 2Z\Omega$ is the Rayleigh discriminant and the prime denotes differentiation with respect to r . In this limit, the boundary conditions reduce to $u_r = 0$ at $r = r_i, r_o$. Equation (2.6) has been solved by a shooting method. The numerical integration is started from both cylinders towards a fitting point r_f using the boundary conditions and an initial guess ω . The Wronskian $W_k = u_r(r_f^+)u_r'(r_f^-) - u_r(r_f^-)u_r'(r_f^+)$ is computed from the two distinct values $(u_r(r_f^+), u_r'(r_f^+))$ and $(u_r(r_f^-), u_r'(r_f^-))$ on either side of r_f . An iterative secant method is used to find the value of ω for which the Wronskian vanishes (Schecter & Montgomery 2004).

Equations (2.1)–(2.5) have been solved by the Chebyshev collocation spectral method (Antkowiak & Brancher 2004; Fabre & Jacquin 2004). The five equations (2.1)–(2.5) are first reduced to three equations for (u_r, u_θ, ρ) , which can be written in the compact form

$$\omega \mathbf{B} \begin{pmatrix} u_r \\ u_\theta \\ \rho \end{pmatrix} = \mathbf{A} \begin{pmatrix} u_r \\ u_\theta \\ \rho \end{pmatrix}, \tag{2.7}$$

where \mathbf{A} and \mathbf{B} are differential operator matrices (for the details, see Park 2012). The continuity equation implies that the boundary condition $u_z = 0$ at $r = r_i, r_o$ transforms to $du_r/dr = 0$ for this reduced system. The linear mapping

$$r = \frac{r_i - r_o}{2} \zeta + \frac{r_i + r_o}{2} \tag{2.8}$$

is used to map the Chebyshev domain $\zeta = 1 \rightarrow -1$ into $r = r_i \rightarrow r_o$. An advantage of this linear mapping is that the collocation points are concentrated near each cylinder so that boundary modes can be easily captured. The number of collocation points for the spectral method is chosen from 80 to 120 points depending on the control parameters. The spurious modes are eliminated by using a convergence criterion based on the spectral residual (Fabre & Jacquin 2004).

The seven control parameters of the problem ($\Omega_i, \Omega_o, r_i, r_o, N, \nu, D$) can be expressed in terms of five independent non-dimensional numbers:

$$\mu = \frac{\Omega_o}{\Omega_i}, \quad \eta = \frac{r_i}{r_o}, \quad F = \frac{\Omega_o}{N}, \quad Re = \frac{\Omega_o r_o (r_o - r_i)}{\nu}, \quad Sc = \frac{\nu}{D}, \tag{2.9}$$

where F is the Froude number, Re the Reynolds number and Sc the Schmidt number. In contrast to Shalybkov & Rüdiger (2005) or Le Dizès & Riedinger (2010), the Froude number and Reynolds number are based on the angular velocity Ω_o of the outer cylinder, since we shall consider the limiting case where the inner cylinder is at rest. For the same reason, it is convenient to use the inverse of the usual velocity ratio μ

$$\lambda = \frac{1}{\mu} = \frac{\Omega_i}{\Omega_o}. \tag{2.10}$$

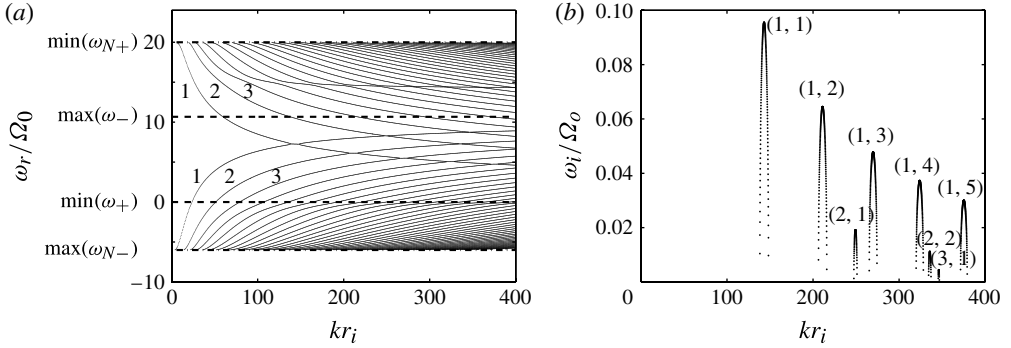


FIGURE 1. (a) Frequency ω_r and (b) growth rate ω_i as functions of the vertical wavenumber kr_i for $\lambda = 0$, $m = 14$, $\eta = 0.8$, $F = 0.05$ and $Re = \infty$. In panel (b), the labels (n_1, n_2) denote the branch number of the first (n_1) and the second family (n_2) indicated in panel (a).

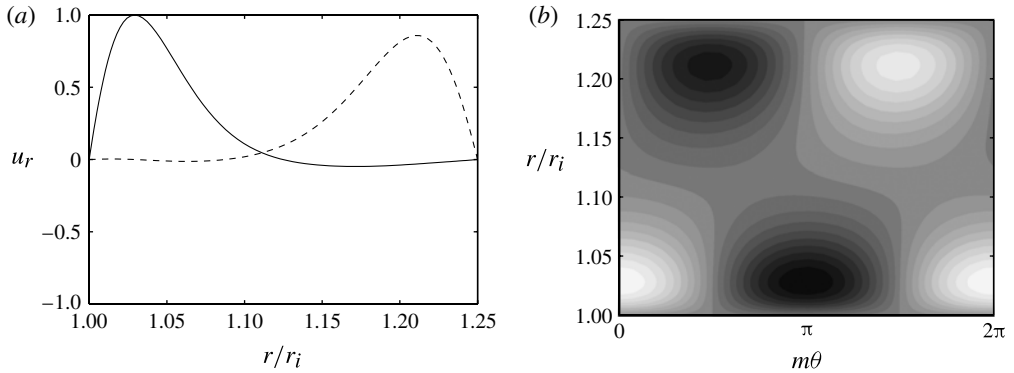


FIGURE 2. (a) Eigenfunction u_r in the radial direction r for $\lambda = 0$, $m = 14$, $\eta = 0.8$, $F = 0.05$, $Re = \infty$ and $kr_i = 143$ corresponding to the maximum of the peak (1, 1) in figure 1(b). The solid and dashed lines are the real and imaginary parts, respectively. (b) Contour plot of the eigenfunction $Re[u_r(r) \exp(im\theta)]$ in the horizontal plane (r, θ) for the same parameters as in panel (a). The contour interval is 0.1.

3. Illustrative example of instability

Figure 1 displays one example of the frequency (figure 1a) and growth rate (figure 1b) when the inner cylinder is at rest, $\lambda = 0$ ($\mu = \infty$), with the gap ratio $\eta = 0.8$, the azimuthal wavenumber $m = 14$, in a strongly stratified inviscid fluid: $F = 0.05$ and $Re = \infty$. Two families of branches can be easily identified in the frequency plot (figure 1a). In each family, there is an infinite number of branches, which can be labelled by the number of oscillations of the radial eigenfunction (indicated for the first three branches of each family in figure 1a). As seen in figure 1(b), the growth rate is positive in the neighbourhood of each crossing point of the frequency branches. The maximum growth rate is reached in the first band, which corresponds to the crossing of the first branch of each family.

Figure 2 displays the corresponding most unstable eigenmode. We can clearly identify two modes close to each cylinder interacting with an azimuthal phase shift around $\pi/2$ (figure 2b). This structure is reminiscent of the SRI one that consists of

two boundary trapped waves on each cylinder (Yavneh *et al.* 2001; Molemaker *et al.* 2001). In the next section, we show that these two family of modes correspond to inertia–gravity waves.

4. Asymptotics and instability mechanism

In the example shown in the previous section, the instability occurs for axial wavenumbers kr_i larger than 140. Therefore, in order to describe the instability, it is interesting to use a WKBJ analysis for large axial wavenumber k following Billant & Le Dizès (2009), Le Dizès & Billant (2009) and Le Dizès & Riedinger (2010). This will allow us to explain the instability mechanism and to obtain general necessary conditions for instability.

4.1. The WKBJ approximation

For $k \gg 1$, the solution of the inviscid equation (2.6) can be approximated by (Bender & Orszag 1978)

$$u_r = \frac{Q^{1/2}}{r^{1/2}\beta^{1/4}} \left[A_+ \exp \left(ik \int_{r_i}^r \sqrt{\beta(t)} dt \right) + A_- \exp \left(-ik \int_{r_i}^r \sqrt{\beta(t)} dt \right) \right], \quad (4.1)$$

where A_{\pm} are constants,

$$\beta = \frac{s^2 - \phi}{N^2 - s^2} \quad (4.2)$$

and r_t is a turning point where $\beta(r_t) = 0$. We recall that $s = -\omega + m\Omega$ is the Doppler-shifted frequency and $\phi = 2Z\Omega$ is the Rayleigh discriminant. The WKBJ approximations are wavelike if β is real and positive, while they have an exponential behaviour if $\beta < 0$. In the former case, $l_r = k\sqrt{\beta}$ corresponds to the local radial wavenumber of the waves. When the angular velocity Ω is constant, l_r is constant and (4.2) is nothing but the dispersion relation of inertia–gravity waves in a uniformly rotating and stratified fluid: $s^2 = (N^2 l_r^2 + 4\Omega^2 k^2)/(k^2 + l_r^2)$

Figure 3 shows the sign of β as a function of r and ω for the same parameters as figure 1. The sign of β^2 changes at characteristic frequencies called the epicyclic frequencies $\omega_{\pm}(r) = m\Omega \pm \sqrt{\phi}$ for which $s^2 = \phi$ (Le Dizès & Lacaze 2005), and the critical frequencies $\omega_{N\pm} = m\Omega \pm N$ for which $N^2 = s^2$. These characteristic frequencies generally increase with r since Ω increases with r when the outer cylinder rotates faster than the inner cylinder. Two distinct wave regions (shaded) can be seen in figure 3. Non-singular inertia–gravity waves can exist if their frequency lies in the interval $\max(\omega_{N-}) < \omega < \min(\omega_{N+})$. Just above and below this interval, waves can also exist but they are singular at the critical radius where $|s| = N$ so that they will be damped by diffusive effects. When $\omega_r > \max(\omega_{N+})$ or $\omega_r < \min(\omega_{N-})$, the WKBJ approximations are exponential everywhere so that they cannot satisfy the boundary conditions on both cylinders.

In figure 3(b), the horizontal solid lines show three different examples of frequency ω_r , which can be categorized depending on the number of turning points r_t . The WKBJ approximations can be wavelike throughout the gap $r_i < r < r_o$ like for the frequency labelled *O* in figure 3(b) or they can contain an evanescent region delimited by one or two turning points like for the examples of frequency labelled *I* and *II*, respectively. For each of these configurations, we can derive a dispersion relation by using classical connection formula at the turning points (Bender & Orszag 1978) and by imposing the boundary conditions at $r = r_i, r_o$. These analyses are performed in

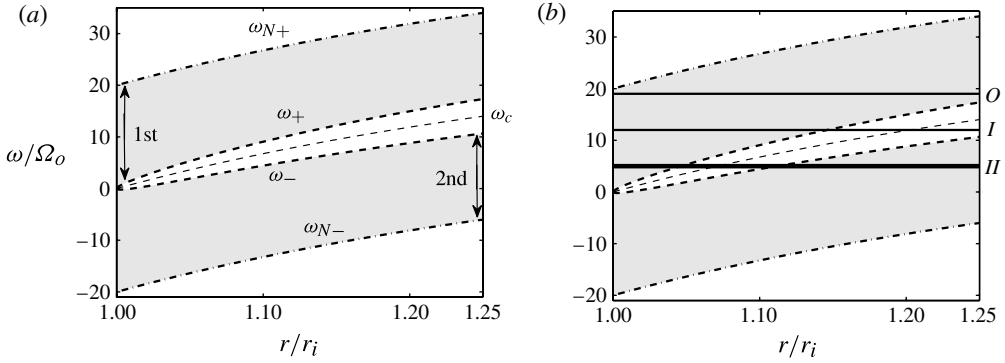


FIGURE 3. Typical example of the sign of β for the same parameters as in figure 1. The epicyclic frequencies ω_{\pm} and the critical frequencies $\omega_{N\pm}$ are plotted by thick dashed and thick dot-dashed lines, respectively. The critical frequency $\omega_c = m\Omega$ at which $s = 0$ is also plotted by dashed lines. The regions where the solutions are wavelike ($\beta > 0$) are shaded. Panel (b) is the same as panel (a) except that solid lines show examples of the frequency ω_r for which there is no turning point (*O*), one turning point (*I*) or two turning points (*II*).

appendix B and we give here only the final results. For the case *O* (no turning point), the dispersion relation is simply

$$\exp\left(2ik \int_{r_i}^{r_o} \sqrt{\beta(t)} dt\right) = 1 \quad \text{leading to} \quad \int_{r_i}^{r_o} \sqrt{\beta(t)} dt = \frac{n\pi}{k}, \quad (4.3)$$

where n is a non-zero integer. For the case *I*, the WKB approximations are wavelike between the inner cylinder r_i and a turning point r_{t1} . The dispersion relation is then

$$K(r_i, r_{t1}) = -i \left[\frac{2 + iX(r_{t1}, r_o)}{2 - iX(r_{t1}, r_o)} \right], \quad (4.4)$$

where

$$K(r_a, r_b) = \exp\left(2ik \int_{r_a}^{r_b} \sqrt{\beta(t)} dt\right), \quad X(r_a, r_b) = \exp\left(-2k \int_{r_a}^{r_b} \sqrt{-\beta(t)} dt\right). \quad (4.5)$$

Alternatively, there exists a configuration (labelled *I'*) where the wave region is enclosed between a turning point r_{t2} and the outer cylinder r_o . This configuration is absent in figure 3 but it exists for other parameter values. The corresponding WKB dispersion relation is

$$K(r_{t2}, r_o) = -i \left[\frac{2 + iX(r_i, r_{t2})}{2 - iX(r_i, r_{t2})} \right]. \quad (4.6)$$

Finally, in case *II*, the evanescent region is enclosed between two turning points r_{t1}, r_{t2} leading to

$$(K(r_i, r_{t1}) + i\alpha)(K(r_{t2}, r_o) + i\alpha) = (1 - \alpha^2)K(r_i, r_{t1})K(r_{t2}, r_o), \quad (4.7)$$

where $\alpha = (4 + X(r_{t1}, r_{t2})) / (4 - X(r_{t1}, r_{t2}))$. Note that these dispersion relations are valid only when the turning points are well separated and sufficiently far from the boundaries. Even if we have illustrated the derivation of the dispersion relations of the different configurations in the particular case of figure 3, we emphasize that they

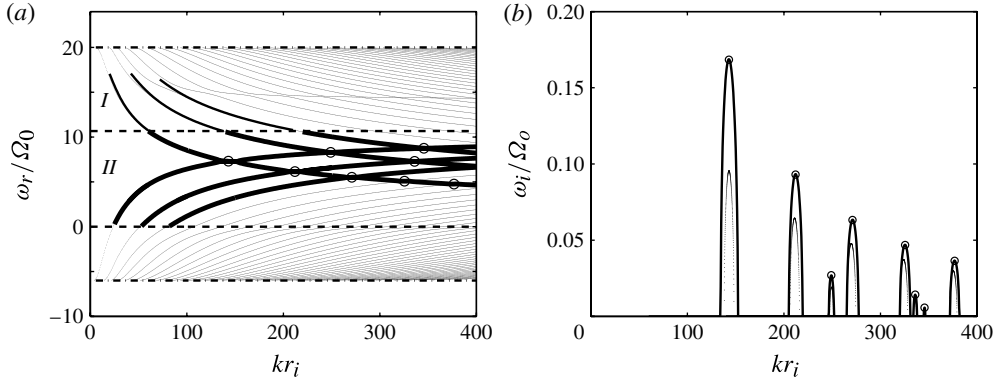


FIGURE 4. Same as figure 1 except that the asymptotic dispersion relations (4.4) for the case I and (4.7) for the case II are also plotted by solid lines. The asymptotic maximum growth rate (4.14) is also shown with empty circles.

are general since only the four configurations (O, I, I', II) are encountered when the parameters are varied.

The asymptotic dispersion relations (4.4) and (4.7) are compared to the numerical results in figure 4, which is otherwise the same as figure 1. We see that the asymptotic and numerical frequencies are always in excellent agreement. The locations of the growth rate peaks are also very well predicted, but their amplitudes tend to be overestimated in the asymptotics. The growth rate is non-zero only in the configuration II, i.e. only when there exists a wave region attached to each cylinder and separated by an evanescent region.

4.2. Detailed asymptotic analysis of the resonance

The instability can be understood further from (4.7) by considering that the evanescent region is large. In this limit, $X(r_{i1}, r_{i2})$ is very small so that α tends to unity. In the limit $\alpha = 1$, (4.7) reduces to

$$(K(r_i, r_{i1}) + i)(K(r_{i2}, r_o) + i) = 0. \tag{4.8}$$

Thus, the dispersion relation is satisfied if either

$$K(r_i, r_{i1}) = -i \quad \text{or} \quad K(r_{i2}, r_o) = -i. \tag{4.9a,b}$$

These two relations correspond to the two distinct families of frequency branches in figures 1(a) and 4(a). Equations (4.9a,b) correspond to neutral waves attached to the inner cylinder and to the outer cylinder, respectively.

Since the instability occurs when two branches cross, we consider now a frequency ω_0 and a vertical wavenumber k_0 where the two dispersion relations (4.9a,b) are satisfied simultaneously. We also consider the first-order correction due to the small parameter $X(r_{i1}, r_{i2})$. Thus, the parameter α reads $\alpha = 1 + \epsilon^2/2 + \dots$, where $\epsilon = \sqrt{X(r_{i1_0}, r_{i2_0})}$ and where quantities with a subscript 0 are evaluated with the leading-order frequency ω_0 and wavenumber k_0 . Similarly, the frequency ω and vertical wavenumber k can be expanded in the form

$$\omega = \omega_0 + \epsilon\omega_1 + \epsilon^2\omega_2 + \dots, \tag{4.10a}$$

$$k = k_0 + \epsilon k_1 + \epsilon^2 k_2 + \dots. \tag{4.10b}$$

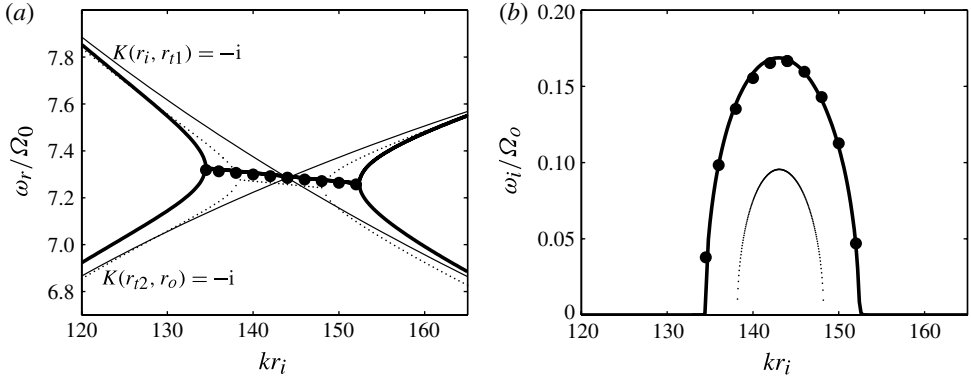


FIGURE 5. (a) Frequency and (b) growth rate as functions of the vertical wavenumber kr_i around the resonance (1, 1) between the first branches of each family for the same parameters as in figure 4. The dotted and solid thin lines are numerical results and asymptotic results from (4.9), respectively. The thick solid lines show the asymptotic dispersion relation (4.7), and filled circles show (4.13).

The dispersion relation (4.7) then reduces to (4.8) at leading order in ϵ . The order $O(\epsilon)$ is satisfied identically, and at order $O(\epsilon^2)$ we have

$$[k_1 h(r_i, r_{i1_0}) + k_0 \omega_1 h_\omega(r_i, r_{i1_0})][k_1 h(r_{i2_0}, r_o) + k_0 \omega_1 h_\omega(r_{i2_0}, r_o)] = \frac{1}{4}, \quad (4.11)$$

where

$$h(r_a, r_b) = \int_{r_a}^{r_b} \sqrt{\beta_0} dt, \quad h_\omega(r_a, r_b) = \int_{r_a}^{r_b} \frac{\partial \sqrt{\beta_0}}{\partial \omega} dt, \quad (4.12)$$

and $\beta_0 = (s_0^2 - \phi)(N^2 - s_0^2)$ with $s_0 = -\omega_0 + m\Omega$. This gives ω_1 as

$$\omega_1 = -\frac{k_1}{2k_0} \left(\frac{h(r_i, r_{i1_0})}{h_\omega(r_i, r_{i1_0})} + \frac{h(r_{i2_0}, r_o)}{h_\omega(r_{i2_0}, r_o)} \right) \pm \frac{1}{2k_0} \sqrt{\left(\frac{h(r_i, r_{i1_0})}{h_\omega(r_i, r_{i1_0})} - \frac{h(r_{i2_0}, r_o)}{h_\omega(r_{i2_0}, r_o)} \right)^2 k_1^2 + \frac{1}{h_\omega(r_i, r_{i1_0})h_\omega(r_{i2_0}, r_o)}}. \quad (4.13)$$

From (4.13), we see that a necessary and sufficient condition for instability (i.e. ω_1 imaginary) is that $h_\omega(r_i, r_{i1_0})h_\omega(r_{i2_0}, r_o) < 0$. In this case, the maximum growth rate is reached when $k_1 = 0$ and is

$$\omega_{i,max} = \text{Im}(\epsilon\omega_1) = \frac{\sqrt{X(r_{i1_0}, r_{i2_0})}}{2k_0} \sqrt{\frac{-1}{h_\omega(r_i, r_{i1_0})h_\omega(r_{i2_0}, r_o)}}. \quad (4.14)$$

As seen by the symbols in figure 4(b), the growth rate (4.14) coincides almost exactly with the maximum of the peaks predicted by (4.7). In figure 5, a close-up view of the region around the resonance (1, 1) between the first branches of each family is shown. We can clearly see that the resonance occurs when the frequency of the two families of waves (4.9a) and (4.9b) cross. The asymptotic frequency and growth rate from (4.13) are almost superimposed onto those from the asymptotic dispersion relation (4.7).

Therefore, a sufficient condition for instability is that $\partial\sqrt{\beta_0}/\partial\omega$ is of opposite sign in the intervals $[r_i, r_{t1_0}]$ and $[r_{t2_0}, r_o]$. As shown in Le Dizès & Billant (2009), the quantity $\partial\sqrt{\beta_0}/\partial\omega$ is related to the radial group velocity of the waves. The local radial wavenumber of the first term in the WKBJ approximation (4.1) is $l_r = k_0\sqrt{\beta_0}$, so that the group velocity is indeed

$$v_g = \frac{\partial\omega}{\partial l_r} = 1 / \left(k_0 \frac{\partial\sqrt{\beta_0}}{\partial\omega} \right). \quad (4.15)$$

Hence, the condition for instability is that the group velocity of the first WKBJ approximation in (4.1) is reversed between the two intervals $[r_i, r_{t1_0}]$ and $[r_{t2_0}, r_2]$. In other words, a wave propagating radially inwards for $r < r_{t1_0}$ transforms to a wave propagating outwards for $r > r_{t2_0}$ so that the evanescent region acts a wave source. Since $\partial\sqrt{\beta_0}/\partial\omega = s_0(\phi - N^2)/(\sqrt{\beta_0}(N^2 - s_0^2)^2)$, this requires that there exists a critical point r_c where $s_0(r_c) = 0$ between the two turning points r_{t1_0} and r_{t2_0} . As seen in figure 3, this is indeed the case since the critical frequency $\omega_c = m\Omega$ is enclosed between the epicyclic frequencies ω_- and ω_+ . A similar instability condition has been derived by Le Dizès & Billant (2009) for the radiative instability.

The instability can also be explained in terms of over-reflection (Lindzen, Farrell & Tung 1980; Takehiro & Hayashi 1992; Billant & Le Dizès 2009; Le Dizès & Billant 2009). When $\max(\omega_{N-}) < \omega_r < \min(\omega_{N+})$ and $N^2 > \phi$, the first WKBJ approximation in (4.1) corresponds for $r < r_{t1}$ to a wave propagating towards r_{t1} since its group velocity is positive because $s < 0$. Conversely, the second term of (4.1) corresponds to the reflected wave at r_{t1} . The reflection coefficient at r_{t1} is therefore $\mathcal{R}_1 = |A_-^2/A_+^2|$. Furthermore, the boundary condition at $r = r_i$ implies that

$$\mathcal{R}_1 = 1/|K^2(r_i, r_{t1})|. \quad (4.16)$$

For $r > r_{t2}$, the group velocity is reversed so that the reflection coefficient at r_{t2} is $\mathcal{R}_2 = |A_+^2/A_-^2|$ and, similarly, the boundary condition at $r = r_o$ implies that

$$\mathcal{R}_2 = |K^2(r_{t2}, r_o)|. \quad (4.17)$$

The previous asymptotic analysis for $\alpha = 1 + \epsilon^2/2 + \dots$ shows that, when $k_1 = 0$,

$$K(r_i, r_{t1}) = K_0(r_i, r_{t1_0})[1 + 2ik_0\epsilon\omega_1 h_\omega(r_i, r_{t1_0}) + O(\epsilon^2)], \quad (4.18a)$$

$$K(r_{t2}, r_o) = K_0(r_{t2_0}, r_o)[1 + 2ik_0\epsilon\omega_1 h_\omega(r_{t2_0}, r_o) + O(\epsilon^2)]. \quad (4.18b)$$

Since $h_\omega(r_i, r_{t1_0}) > 0$, $h_\omega(r_{t2_0}, r_o) < 0$ and $|K_0(r_i, r_{t1_0})| = |K_0(r_{t2_0}, r_o)| = 1$, we see that $|K(r_i, r_{t1})|$ is less than one, whereas $|K(r_{t2}, r_o)|$ is greater than one. Hence, the reflection coefficients \mathcal{R}_1 and \mathcal{R}_2 are both greater than one, meaning that incident waves are over-reflected at the turning points r_{t1} and r_{t2} .

In contrast, when there is a single turning point, the dispersion relations (4.4) and (4.6) imply that $|K(r_i, r_{t1})| = 1$ and $|K(r_{t2}, r_o)| = 1$. Therefore, there is no over-reflection, explaining why the waves are neutral in this case.

4.3. Frequency bands and instability conditions

In the previous section, we have found that, when the evanescent region is large, there exist two decoupled dispersion relations (4.9a,b). They can be rewritten as

$$\int_{r_i}^{r_{t1}} \sqrt{\beta(t)} dt = \left(n - \frac{1}{4} \right) \frac{\pi}{k}, \quad (4.19a)$$

$$\int_{r_{i2}}^{r_o} \sqrt{\beta(t)} dt = \left(n - \frac{1}{4}\right) \frac{\pi}{k}, \tag{4.19b}$$

where n is a non-negative integer. These relations are valid as long as there exists at least one turning point. In the absence of a turning point, the dispersion relation (4.3) should be used.

The two dispersion relations (4.19) show clearly that there exist two independent families of waves: one trapped between the inner cylinder r_i and $\min(r_{i1}, r_o)$; and the other trapped between $\min(r_{i2}, r_i)$ and the outer cylinder r_o . As seen in figure 3(a), the first family can exist in the frequency interval

$$\min(\omega_+) < \omega < \min(\omega_{N+}), \tag{4.20}$$

while the second can exist if the frequency lies in the range

$$\max(\omega_{N-}) < \omega < \max(\omega_-). \tag{4.21}$$

These two distinct frequency bands correspond exactly to those of the two branch families in figure 1(a). The frequency of the first family starts from $\omega = \min(\omega_{N+})$ and decreases to $\omega = \min(\omega_+)$ as k increases, whereas the frequency of the second family increases from $\omega = \max(\omega_{N-})$ to $\omega = \max(\omega_-)$ as k increases.

The main conditions for instability can be derived from the frequency ranges (4.20) and (4.21). First, the conditions for the existence of the two wave families, $\max(\omega_{N-}) < \max(\omega_-)$ and $\min(\omega_+) < \min(\omega_{N+})$, imply that

$$F < \frac{1}{2} \sqrt{\frac{1 - \eta^2}{1 - \lambda \eta^2}}. \tag{4.22}$$

Therefore, the fluid should be strongly stratified: the critical Froude number is always less than 1/2 for $0 \leq \lambda < 1$. The condition (4.22) only applies when $\lambda < 1$. When $\lambda \geq 1$, as shown in appendix A, the critical Froude number is larger than 1/2, so that the instability occurs for weaker stratification than for $\lambda < 1$.

Since the instability requires that the branches cross, a second condition is that the two frequency bands (4.20) and (4.21) share a common interval. This requires that $\max(\omega_-) > \min(\omega_+)$ and $\min(\omega_{N+}) > \max(\omega_{N-})$, leading to the following conditions for instability:

$$\frac{2}{|1 - \sqrt{\lambda}|} \sqrt{\frac{1 - \lambda \eta^2}{1 - \eta^2}} < m < \frac{2}{F|1 - \lambda|}. \tag{4.23}$$

Note that these inequalities also apply when $\lambda > 1$, as discussed in appendix A. This relation shows that only a finite band of azimuthal wavenumbers m are able to satisfy the resonance condition: for example, for the parameters of figure 1, (4.23) gives $10/3 < m < 40$.

5. Parametric study

We now study numerically the maximum growth rate of the instability as a function of the main parameters: m , F , η , Re and λ in the range $0 \leq \lambda < 1$. The instability conditions derived in the previous section will be tested.

5.1. Variation with the azimuthal wavenumber m

Figure 6 displays the maximum growth rate as a function of the azimuthal wavenumber for the same control parameters as in figure 1. It is confirmed that

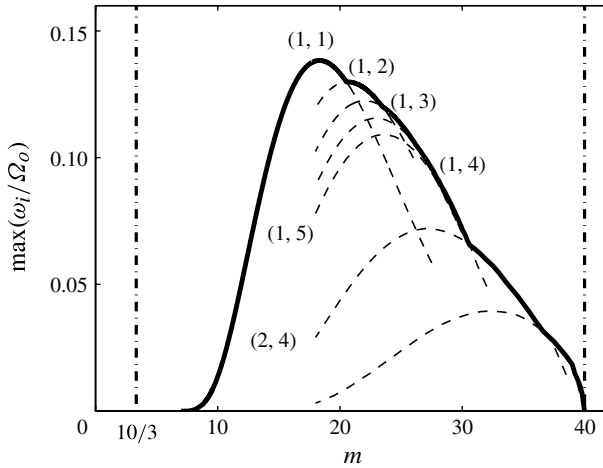


FIGURE 6. Maximum growth rate (bold line) as a function of the azimuthal wavenumber m for $\lambda = 0$, $\eta = 0.8$, $F = 0.05$ and $Re = \infty$. Dashed lines represent the maximum growth rates of the resonance (n_1, n_2) , where n_1 and n_2 are the branch number of each family (see figure 1a). Bold dot-dashed lines indicate bounds given by (4.23).

the maximum growth rate is positive only when m belongs to the interval (4.23). The upper azimuthal wavenumber cut-off corresponds exactly to the upper bound predicted by (4.23). The lower cut-off seems to be around $m \approx 8$, i.e. higher than the lower bound of (4.23). However, the growth rate is exponentially small but non-zero for the azimuthal wavenumbers $4 < m < 8$ because the evanescent region is very large. The growth rate curve reaches a maximum for $m \approx 18$ and exhibits a broken shape because the dominant resonance is not always between the first branch of each family (1, 1) but can involve the following branches as indicated in figure 6. The lower bound in (4.23) is always larger than $m = 2$ for $0 \leq \lambda < 1$ and increases to infinity as λ tends to unity. The unstable azimuthal wavenumbers are therefore typically larger than for $1 < \lambda < 1/\eta^2$ since the lower bound of (4.23) goes to zero when $\lambda \rightarrow 1/\eta^2$ (Molemaker *et al.* 2001; Yavneh *et al.* 2001; Le Dizès & Riedinger 2010).

5.2. Effect of the Froude number F

Figure 7(a) shows the maximum growth rate as a function of the azimuthal wavenumber m for $\eta = 0.8$, $\lambda = 0$ and $Re = \infty$ for different Froude numbers. The band of unstable azimuthal wavenumbers widens towards large azimuthal wavenumbers when the Froude number decreases. The upper azimuthal wavenumber cut-off agrees well with the upper bound predicted by (4.23). The lower azimuthal wavenumber cut-off does not vary with the Froude number, in agreement with (4.23). The maximum growth rate and most amplified azimuthal wavenumber are almost constant and equal to $\max(\omega_i/\Omega_o) \approx 0.14$ and $m_{max} \approx 18$ when $F \lesssim 0.05$, whereas they strongly decrease when F is increased above 0.1 because the upper azimuthal wavenumber cut-off is then lower than or comparable to $m_{max} = 18$. The evolution of the maximum growth rate as a function of F is summarized in figure 7(b). The maximum growth rate seems to go to zero around the Froude number $F \approx 0.2$, which is smaller than the critical Froude number $F_c = 0.3$ predicted by (4.22). However, the growth rate is likely to be very small but non-zero for $0.2 \lesssim F \leq F_c$ because the evanescent region is very large.

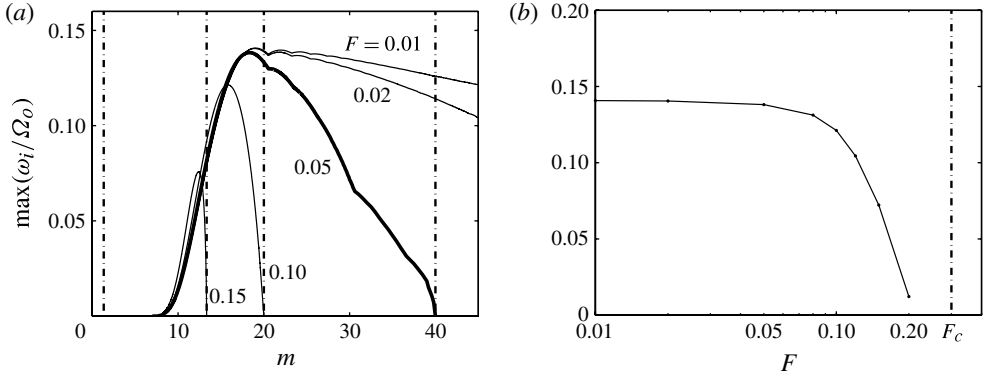


FIGURE 7. (a) Maximum inviscid growth rate as a function of the azimuthal wavenumber m for different Froude numbers $F = [0.01, 0.02, 0.05, 0.1, 0.15]$ for $\lambda = 0$ and $\eta = 0.8$. The dashed-dotted lines represent the bound given by (4.23). (b) Maximum growth rate as a function of the Froude number F for $\eta = 0.8$ and $\lambda = 0$. The critical Froude number F_c given by (4.22) is shown by a dashed-dotted line.

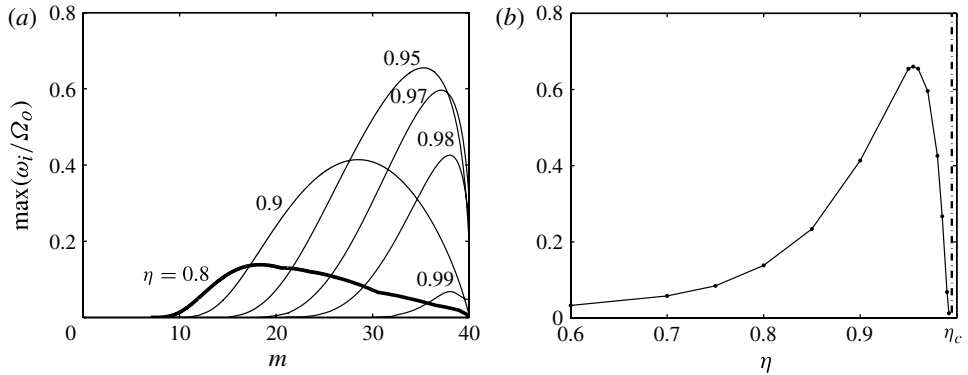


FIGURE 8. (a) Maximum inviscid growth rate as a function of the azimuthal wavenumber m for different gap ratios $\eta = [0.8, 0.9, 0.95, 0.97, 0.98, 0.99]$ for $F = 0.05$ and $\lambda = 0$. (b) Maximum growth rate as a function of the gap ratio η for $F = 0.05$ and $\lambda = 0$. The critical gap ratio η_c is shown by a dashed-dotted line.

5.3. Effect of the gap ratio η

Figure 8(a) shows the maximum growth rate as a function of the azimuthal wavenumber for $F = 0.05$, $\lambda = 0$ and $Re = \infty$ for different gap ratios η . When η increases, the band of unstable azimuthal wavenumbers shrinks because the lower cut-off increases whereas the upper cut-off remains constant, in agreement with (4.23). Nevertheless, we note that the growth rate is not always strictly zero at the upper cut-off $m_c = 40$. This is because this critical azimuthal wavenumber corresponds only to the limit above which the modes have a singularity at the critical point r_N where $|s(r_N)| = N$. The modes thereby start to be damped for $m > m_c$, but if the destabilizing effect due to the resonance is stronger than this damping, the growth rate can remain positive for $m > m_c$. In practice, however, we see that the growth rate decays abruptly near $m = m_c$ and should vanish only slightly above m_c . The maximum

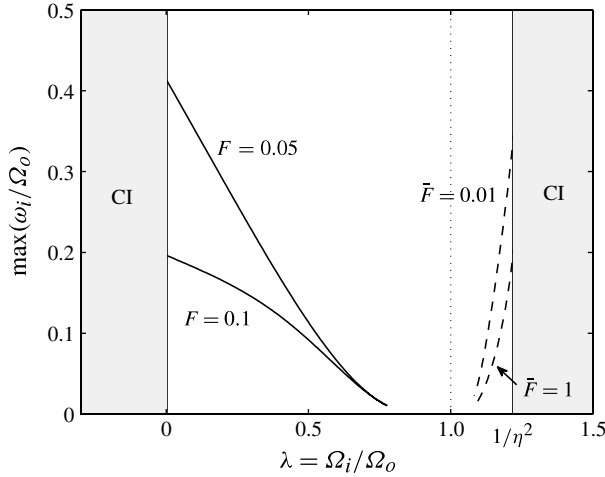


FIGURE 9. Maximum inviscid growth rates of the SRI as a function of $\lambda = 1/\mu = \Omega_i/\Omega_o$ for the Froude numbers $F = 0.05, 0.1$ and for $\eta = 0.9$ (solid lines). Dashed lines show the results of figure 1 of Molemaker *et al.* (2001) for $\eta = 0.9048$ and Froude numbers $\bar{F} = 0.01, 1$. Note that the Froude number \bar{F} defined by Molemaker *et al.* (2001) is based on the angular velocity $\bar{\Omega}$ at the middle point $\bar{r} = (r_o + r_i)/2$ and is thus slightly different from the present definition. The regimes of the CI are shaded. The dotted line indicates the limit of solid-body rotation $\lambda = 1$.

growth rate first increases with η , but after $\eta > 0.95$ it decreases abruptly. Figure 8(b) summarizes the evolution of the maximum growth rate as a function of the gap ratio η for the same parameters as in figure 8(a). The overall maximum growth rate is reached around $\eta_{max} \approx 0.955$. Then, the maximum growth rate goes abruptly to zero for $\eta = \eta_c = \sqrt{(1 - 4F^2)/(1 - 4\lambda F^2)} = 0.995$ as predicted by (4.22).

5.4. Effect of the angular velocity ratio λ

Figure 9 shows the maximum growth rate as a function of $\lambda = 1/\mu$ for two different values of F for $\eta = 0.9$. In the range investigated in this paper ($0 < \lambda < 1$), the growth rate is maximum when the inner cylinder is at rest ($\lambda = 0$), and decreases to zero as λ increases to unity. The domains of the other instabilities are also indicated in figure 9. The intervals $\lambda < 0$ and $\lambda > 1/\eta^2$ correspond to the domain of the CI. The interval $1 < \lambda < 1/\eta^2$ is the domain of the SRI previously found by Molemaker *et al.* (2001) and Yavneh *et al.* (2001). The growth rate obtained by Molemaker *et al.* (2001) for this regime is also plotted with dashed lines. It is maximum for $\lambda = 1/\eta^2$ and decreases to zero as λ decreases to unity. The growth rate values scaled by the angular velocity of the outer cylinder Ω_o are comparable to those for $0 < \lambda < 1$. Taken all together, we can conclude that the range of instability of the stably stratified Taylor–Couette flow is much wider than previously identified: the growth rate is always positive except in the limit of solid-body rotation ($\lambda = 1$). However, it should be noted that the maximum growth rate becomes very small in the neighbourhood of $\lambda = 1$.

These results are actually very similar to those for the radiative instability of a columnar vortex in a stratified rotating fluid (Park & Billant 2012, 2013). In the latter case, the radiative instability exists when the Rossby number is $Ro \geq -1$

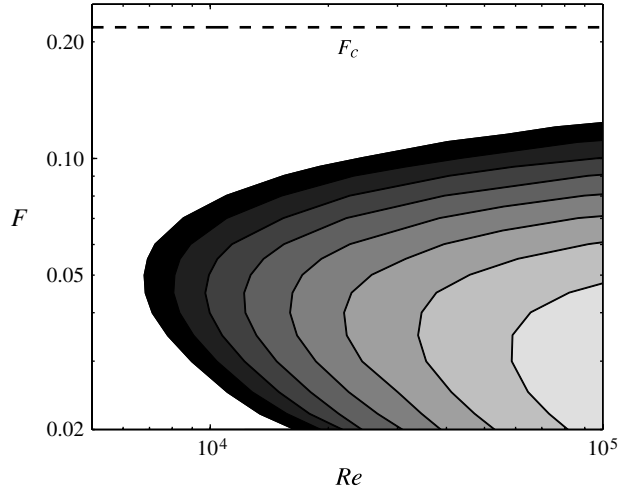


FIGURE 10. Neutral stability curve with contours of maximum growth rate $\max(\omega_i/\Omega_o)$ as a function of the Reynolds number Re and Froude number F for $\eta = 0.9$, $\lambda = 0$ and $Sc = 700$. The unstable domain is shaded and the contour interval is 0.05. The dashed line represents the critical Froude number $F_c = 0.218$ given by (4.22).

and its growth rate is maximum at both ends of this interval, i.e. for $Ro = -1$ and $Ro = +\infty$, and vanishes in the limit $Ro \rightarrow 0$. From the relation (1.2), we see that these three particular values of Ro correspond exactly to those found above for the strato-rotational instability of the stratified Taylor–Couette flow: $\lambda = 0$, $\lambda = 1/\eta^2$ for the growth rate maxima and $\lambda = 1$ for the minimum. Thus, even if the boundary conditions are completely different between the two flows, there is a close correspondence between them and their associated instabilities. This similarity originates from the fact that both the radiative and strato-rotational instabilities are due to an over-reflection of waves between a boundary and an evanescent region. In the case of the radiative instability, there is a single over-reflecting zone in the vicinity of the vortex core (Park & Billant 2012) while for the strato-rotational instability, there are two over-reflecting regions, one attached to each cylinder as seen in § 4.

5.5. Viscous effect

Finally, we have investigated the viscous and diffusive effects for one set of parameters: $\lambda = 0$, $\eta = 0.9$ and Schmidt number $Sc = \nu/D = 700$, where ν is the viscosity and D the diffusivity. This value of the Schmidt number corresponds to that for salt-stratified water generally used in laboratory experiments. Figure 10 shows the maximum growth rate as a function of the Reynolds number $Re = \Omega_o r_o (r_o - r_i)/\nu$ and the Froude number F . The critical Reynolds number Re_c is about $Re_c \approx 7000$ at $F \approx 0.05$. This value of Re_c is higher than the critical values of order $Re_{ic} \sim O(10^3)$, where Re_i is the inner Reynolds number $Re_i = \Omega_i r_i (r_o - r_i)/\nu$, found for $1 < \lambda < 1/\eta^2$ (Yavneh *et al.* 2001; Shalybkov & Rüdiger 2005; Le Bars & Le Gal 2007) because the associated vertical and azimuthal wavenumbers are larger for $0 \leq \lambda < 1$ than for $1 < \lambda < 1/\eta^2$. The corresponding Froude number is also typically one order of magnitude smaller for $0 \leq \lambda < 1$ than for $1 < \lambda < 1/\eta^2$ because of the different conditions (4.23) and (A 2), respectively, applying to these two regimes.

6. Conclusion and discussion

In conclusion, we have discovered that the stratified Taylor–Couette flow is also unstable when the outer cylinder rotates faster than the inner cylinder $d\Omega^2/dr > 0$ (i.e. the angular velocity ratio $\lambda = 1/\mu = \Omega_i/\Omega_o < 1$). Hence, the sufficient condition for inviscid instability $d\Omega^2/dr < 0$ proposed by Yavneh *et al.* (2001) and Molemaker *et al.* (2001) is extended to $d\Omega^2/dr \neq 0$. The instability mechanism involves the resonance of two families of inertia–gravity waves like for the SRI (Molemaker *et al.* 2001; Yavneh *et al.* 2001; Le Dizès & Riedinger 2010). A WKBJ analysis in the inviscid limit shows that this new instability exists only in a given band of relatively large azimuthal wavenumbers and only if the fluid is strongly stratified. The theoretical WKBJ predictions are in very good agreement with the numerical results. The growth rate is independent of the stratification if the Froude number is sufficiently small. In contrast, it depends strongly on the gap ratio $\eta = r_i/r_o$ and is maximum for a value of η close to unity. The growth rate reaches its maximum when the inner cylinder is at rest $\lambda = 0$ ($\mu = \infty$), and its value is comparable to that previously computed for $1 < \lambda < 1/\eta^2$ (Molemaker *et al.* 2001; Yavneh *et al.* 2001; Le Dizès & Riedinger 2010). However, the critical Reynolds number for $\lambda < 1$ is typically larger than that for $1 < \lambda < 1/\eta^2$. In contrast, the critical Froude number is lower for $\lambda < 1$ than for $1 < \lambda < 1/\eta^2$. This implies that experimental tests would require set-ups with large diameters in order to have low Froude and high Reynolds numbers at the same time. For example, in order to establish the critical Reynolds and Froude numbers $Re \approx 7000$ and $F \approx 0.05$ found in §5.5 for $\eta = 0.9$ and $\lambda = 0$, one would need a set-up with a radius of approximately 60 cm if the buoyancy frequency is $N \approx 3.6 \text{ rad s}^{-1}$ corresponding to salt-stratified water over a working depth of 15 cm. Another stratifying agent or gap ratio η might be more favourable but, nevertheless, the required radius is expected to be of order 50 cm rather than of order 5 cm as in the experiments of Le Bars & Le Gal (2007) in the regime $1 < \lambda < 1/\eta^2$. These conditions are however largely fulfilled in geophysical and astrophysical flows, and our study indicates that the strato-rotational instability, which transforms continuously to the radiative instability as the radius of one cylinder goes to infinity (Le Dizès & Riedinger 2010), can operate in a very large variety of conditions. In particular, the new regime of instability is closely related to anticyclonic geophysical vortices in the centrifugally stable regime that are frequently observed in the oceans (Ménèsquen *et al.* 2009). In this case, the vortex core plays the role of the inner cylinder and there is no outer boundary so that the instability is radiative (Park & Billant 2012).

Acknowledgements

This work was supported by the OLA (Oceanic LAYering) project (ANR2011 Blanc SIMI 5-6 012-02), which was directed by L. Hua. We dedicate this paper to her memory.

Appendix A. Conditions for instability in the regime $1 < \lambda < 1/\eta^2$

In this appendix, we derive stability conditions equivalent to (4.22) and (4.23) but in the regime $1 < \lambda < 1/\eta^2$ investigated by Molemaker *et al.* (2001), Yavneh *et al.* (2001) and Le Dizès & Riedinger (2010). The difference with the case $\lambda < 1$ is that the epicyclic and critical frequencies (ω_{\pm} and $\omega_{N\pm}$) decrease with r (figure 11). As before, non-singular inertia–gravity waves exist in the two frequency intervals

$$\max(\omega_{N-}) < \omega < \max(\omega_-), \quad (\text{A } 1a)$$

$$\min(\omega_+) < \omega < \min(\omega_{N+}), \quad (\text{A } 1b)$$

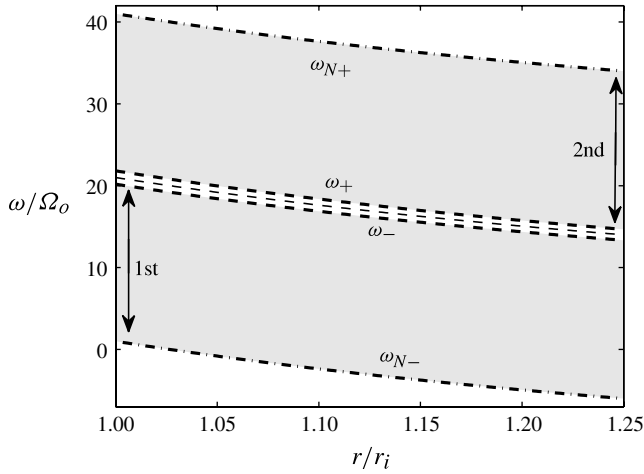


FIGURE 11. Similar to figure 3 except that $\lambda = 1.5$.

but now the condition for the existence of two family of waves is

$$F_i < \frac{1}{2} \sqrt{\frac{\lambda(1 - \eta^2)}{1 - \lambda\eta^2}}, \tag{A 2}$$

where $F_i = \Omega_i/N = \lambda F$ is the Froude number based on the angular velocity of the inner cylinder. In contrast to the regime $\lambda < 1$, the critical Froude number $F_{i,c}$ is always larger than $1/2$ for $1 < \lambda < 1/\eta^2$ and even goes to infinity as $\lambda \rightarrow 1/\eta^2$, so that the instability exists for weaker stratification than in the regime $\lambda < 1$. The band of unstable azimuthal wavenumber remains the same as (4.23). In this case, the lower cut-off goes to zero when $\lambda \rightarrow 1/\eta^2$.

Appendix B. Turning point analysis

In this appendix, we perform an analysis that connects the WKBJ approximations of each different region across the turning points. There exist at most two turning points r_{t1} and r_{t2} with $r_{t1} < r_{t2}$ enclosing an evanescent region $r_{t1} < r < r_{t2}$ (see § 4.1). We assume that the two turning points are well separated from each other and from the cylinders $r = r_i, r_o$.

In the first wave region $r_i < r < r_{t1}$, the WKBJ approximation reads

$$u_r = \frac{Q^{1/2}}{r^{1/2}\beta^{1/4}} \left[A_+ \exp\left(ik \int_{r_{t1}}^r \sqrt{\beta(t)} dt\right) + A_- \exp\left(-ik \int_{r_{t1}}^r \sqrt{\beta(t)} dt\right) \right], \tag{B 1}$$

where A_+ and A_- are constants. As shown in § 4.1, the group velocity (4.15) of the first term of (B 1) is positive so that it corresponds to an incident wave towards the turning point r_{t1} . Conversely, the second term corresponds to a reflected wave from r_{t1} . Around the turning point r_{t1} where the WKBJ approximation (B 1) is no longer valid, (2.6) approximates at leading order to

$$\frac{d^2 u_r}{d\tilde{r}^2} - \tilde{r} u_r = O(\epsilon), \tag{B 2}$$

where $\tilde{r} = (r - r_{i1})/\epsilon$ and $\epsilon = 1/[\beta'(r_{i1})k^2]^{1/3}$. The solution of (B 2) is $u_r = a_1\text{Ai}(\tilde{r}) + b_1\text{Bi}(\tilde{r})$, where a_1 and b_1 are constants and Ai and Bi denote the Airy functions. From the asymptotic behaviours of the Airy functions for $\tilde{r} \rightarrow -\infty$ and $\tilde{r} \rightarrow +\infty$, we obtain the matching WKB approximation for $r > r_{i1}$ as

$$u_r = \frac{Q^{1/2}e^{-i\pi/4}}{r^{1/2}(-\beta)^{1/4}} \left[B_+ \exp\left(-k \int_{r_{i1}}^r \sqrt{-\beta(t)} dt\right) + B_- \exp\left(k \int_{r_{i1}}^r \sqrt{-\beta(t)} dt\right) \right], \quad (\text{B } 3)$$

where $B_+ = (A_+ + iA_-)/2$ and $B_- = iA_+ + A_-$. In the configuration *I*, the second turning point r_{i2} does not exist and the asymptotic dispersion relation (4.4) is obtained by imposing the boundary conditions $u_r = 0$ at $r = r_i, r_o$ in the approximations (B 1) and (B 3). When the turning point $r = r_{i2}$ is present, (B 3) is again not valid in its neighbourhood but a local equation similar to (B 2) can be derived. Its solution is $u_r = c_1\text{Ai}(-\tilde{r}) + d_1\text{Bi}(-\tilde{r})$, where c_1 and d_1 are constants. From the asymptotic behaviours of these Airy functions, we obtain the WKB approximation for $r > r_{i2}$ as

$$u_r = \frac{Q^{1/2}}{r^{1/2}\beta^{1/4}} \left[C_+ \exp\left(ik \int_{r_{i2}}^r \sqrt{\beta(t)} dt\right) + C_- \exp\left(-ik \int_{r_{i2}}^r \sqrt{\beta(t)} dt\right) \right], \quad (\text{B } 4)$$

where $C_+ = (Y^2/2)B_+ - (i/Y^2)B_-$, $C_- = B_-/Y^2 - (iY^2/2)B_+$ and $Y = X(r_{i1}, r_{i2})$, where X is defined in (4.5). As explained in §4.1, the first term of (B 4) now has a negative group velocity and so corresponds to an incident wave towards the turning point r_{i2} , whereas the second term corresponds to a reflected wave. Functions C_+ and C_- can also be expressed in terms of A_+ and A_- as

$$\left. \begin{aligned} C_+ &= \left(\frac{Y^2}{4} + \frac{1}{Y^2}\right)A_+ + i\left(\frac{Y^2}{4} - \frac{1}{Y^2}\right)A_-, \\ C_- &= i\left(\frac{Y^2}{4} - \frac{1}{Y^2}\right)A_+ + \left(\frac{Y^2}{4} + \frac{1}{Y^2}\right)A_-. \end{aligned} \right\} \quad (\text{B } 5)$$

Imposing the boundary conditions in the approximations (B 1), (B 4) and (B 5) leads to the asymptotic dispersion relation (4.7) for the unstable case *II*. When the turning point r_{i1} does not exist (configuration *I*), the asymptotic dispersion relation (4.6) is obtained by imposing the boundary conditions $u_r = 0$ in the approximations (B 4) and (B 3) in which r_{i1} is replaced by r_i .

REFERENCES

- ANDERECK, C. D., LIU, S. S. & SWINNEY, H. L. 1986 Flow regimes in a circular Couette system with independently rotating cylinders. *J. Fluid Mech.* **164**, 155–183.
- ANTKOWIAK, A. & BRANCHER, P. 2004 Transient energy growth for the Lamb–Oseen vortex. *Phys. Fluids* **16**, L1–L4.
- BENDER, C. M. & ORSZAG, S. A. 1978 *Advanced Mathematical Methods for Scientists and Engineers*. McGraw-Hill.
- BILLANT, P. & GALLAIRE, F. 2005 Generalized Rayleigh criterion for non-axisymmetric centrifugal instabilities. *J. Fluid Mech.* **542**, 365–379.
- BILLANT, P. & LE DIZÈS, S. 2009 Waves on a columnar vortex in a strongly stratified fluid. *Phys. Fluids* **21**, 106602.
- BOUBNOV, B. M., GLEDZER, E. B. & HOPFINGER, E. J. 1995 Stratified circular Couette flow: instability and flow regimes. *J. Fluid Mech.* **292**, 333–358.
- CATON, F., JANIAUD, B. & HOPFINGER, E. J. 2000 Stability and bifurcations in stratified Taylor–Couette flow. *J. Fluid Mech.* **419**, 93–124.

- DUBRULLE, B., DAUCHOT, O., DAVIAUD, F., LONGARETTI, P.-Y., RICHARD, D. & ZAHN, J.-P. 2005a Stability and turbulent transport in Taylor–Couette flow from analysis of experimental data. *Phys. Fluids* **17**, 095103.
- DUBRULLE, B., MARIÉ, L., NORMAND, C., RICHARD, D., HERSANT, F. & ZAHN, J. P. 2005b An hydrodynamic shear instability in stratified disks. *Astron. Astrophys.* **429**, 1–13.
- FABRE, D. & JACQUIN, L. 2004 Viscous instabilities in trailing vortices at large swirl numbers. *J. Fluid Mech.* **500**, 239–262.
- HUA, B. L., LE GENTIL, S. & ORLANDI, P. 1997a First transitions in circular Couette flow with axial stratification. *Phys. Fluids* **9**, 365–375.
- HUA, B. L., MOORE, D. W. & LE GENTIL, S. 1997b Inertial nonlinear equilibration of equatorial flows. *J. Fluid Mech.* **331**, 345–371.
- LE BARS, M. & LE GAL, P. 2007 Experimental analysis of the stratorotational instability in a cylindrical Couette flow. *Phys. Rev. Lett.* **99**, 064502.
- LE DIZÈS, S. & BILLANT, P. 2009 Radiative instability in stratified vortices. *Phys. Fluids* **21**, 096602.
- LE DIZÈS, S. & LACAZE, L. 2005 An asymptotic description of vortex Kelvin modes. *J. Fluid Mech.* **542**, 69–96.
- LE DIZÈS, S. & RIEDINGER, X. 2010 The strato-rotational instability of Taylor–Couette and Keplerian flows. *J. Fluid Mech.* **660**, 147–161.
- LINDZEN, R. S., FARRELL, B. & TUNG, K.-K. 1980 The concept of wave overreflection and its application to baroclinic instability. *J. Atmos. Sci.* **37**, 44–63.
- MÉNESGUEN, C., HUA, B. L., PAPENBERG, C., KLAESCHEN, D., GÉLI, L. & HOBBS, R. 2009 Effect of bandwidth on seismic imaging of rotating stratified turbulence surrounding an anticyclonic eddy from field data and numerical simulations. *Geophys. Res. Lett.* **36**, L00D05.
- MOLEMAKER, M. J., MCWILLIAMS, J. C. & YAVNEH, I. 2001 Instability and equilibration of centrifugally stable stratified Taylor–Couette flow. *Phys. Rev. Lett.* **86**, 5270–5273.
- OYOYAMA, K. 1966 On the stability of the baroclinic circular vortex: a sufficient criterion for instability. *J. Atmos. Sci.* **23**, 43–53.
- PARK, J. 2012 Waves and instabilities on vortices in stratified and rotating fluids. PhD thesis, Ecole Polytechnique.
- PARK, J. & BILLANT, P. 2012 Radiative instability of an anticyclonic vortex in a stratified rotating fluid. *J. Fluid Mech.* **707**, 381–392.
- PARK, J. & BILLANT, P. 2013 Instabilities and waves on a columnar vortex in a strongly-stratified and rotating fluid. *Phys. Fluids* (submitted).
- RIEDINGER, X., LE DIZÈS, S. & MEUNIER, P. 2011 Radiative instability of the flow around a rotating cylinder in a stratified fluid. *J. Fluid Mech.* **672**, 130–146.
- RIEDINGER, X., MEUNIER, P. & LE DIZÈS, S. 2010 Instability of a vertical columnar vortex in a stratified fluid. *Exp. Fluids* **49**, 673–681.
- SCHECTER, D. A. & MONTGOMERY, M. T. 2004 Damping and pumping of a vortex Rossby wave in a monotonic cyclone: critical layer stirring versus inertia–buoyancy wave emission. *Phys. Fluids* **26** (5), 1334–1348.
- SHALYBKOV, D. & RÜDIGER, G. 2005 Stability of density-stratified viscous Taylor–Couette flows. *Astron. Astrophys.* **438**, 411–417.
- TAKEHIRO, S. & HAYASHI, Y. 1992 Over-reflection and shear instability in a shallow-water model. *J. Fluid Mech.* **236**, 259–279.
- VANNESTE, J. & YAVNEH, I. 2007 Unbalanced instabilities of rapidly rotating stratified shear flows. *J. Fluid Mech.* **584**, 373–396.
- WITHJACK, E. M. & CHEN, C. F. 1974 An experimental study of Couette instability of stratified fluids. *J. Fluid Mech.* **66**, 725–737.
- YAVNEH, I., MCWILLIAMS, J. C. & MOLEMAKER, M. J. 2001 Non-axisymmetric instability of centrifugally stable stratified Taylor–Couette flow. *J. Fluid Mech.* **448**, 1–21.